


PAPER

[View Article Online](#)
[View Journal](#) | [View Issue](#)Cite this: *Dalton Trans.*, 2025, **54**,
13909Stable zero-dimensional hybrid indium-based
halides with yellow to orange light emissionHong-Zhao Zan,^{a,b} Xiao-Zhong Wang,^b Hai-Xin Zhao,^b Shou-Wang Wang,^b
Lei Chen,^b Hao-Yuan Wang,^b Lai-Zhi Zhao,^b Xiao-De Zhang^b and
Xiang-Wen Kong ^{*b}

Low-dimensional organic–inorganic hybrid materials (OIHMs) in the field of luminescence have been occupying promising application prospects, but the toxicity and instability of lead-based halides are huge obstacles to the industrial utilization of these materials. Developing lead-free halides with low-toxicity and high stability have become important topics of research in recent years. Herein, we report three 0D In-based OIHMs (ABI)₃(InBr₆)Br (ABI = 2-aminium benzo-imidazole) **1**, (DMA)₄(InBr₆)Br (DMA = dimethyl-ammonium) **2**, and (BAPP)(InBr₆)Br·6H₂O (BAPP = 1,4-bis(3-aminopropyl)piperazine) **3**, which show maximum emission peaks within 605–622 nm, with a photoluminescence quantum yield (PLQY) of 60.80% being the highest achieved. More significantly, after one week of immersion in various organic solvents, these halides exhibit no structural degradation with their luminous intensity being well maintained. In addition, halide **1** as a yellow phosphor is used in the preparation of white light-emitting diodes (LEDs) with a high colour rendering index (CRI) of 90.3. This work provides new ideas and strategies for lead-free-based OIHMs in the field of optoelectronic materials.

Received 12th June 2025,
Accepted 31st July 2025

DOI: 10.1039/d5dt01382h

rsc.li/dalton

1. Introduction

3D inorganic hybrid metal halides with the generic formula APbX₃ (where A = Cs⁺ and X = Cl[−], Br[−], I[−]) have attracted broad attention due to outstanding absorption coefficients, high PLQYs, adjustable optical bandgaps, large Stokes shifts, *etc.*^{1–3} However, the toxicity and inconsistent performance of Pb²⁺-based halides have significantly impeded their subsequent applications and development.^{4–6} Recently, low-dimensional OIHMs, which utilize organic cations to substitute for APbX₃ inorganic A-site ions,^{7,8} have garnered significant interest from researchers owing to their adaptable structures and diverse optical applications, including the fabrication of LEDs, X-ray scintillators, photovoltaic sensors, and lasers.^{9–16} Furthermore, OIHMs rely on the structural variety of organic cations and the prevalence of inorganic anions inside various low-dimensional crystal structures (0D, 1D, and 2D), resulting in tuneable photoluminescent properties.^{17–20} Compared to 3D OIHMs, the architecture of 0D halides imparts enhanced quantum

localization effects and exciton confinement energies, leading to effective self-trapped exciton (STE) luminescence and substantial Stokes shifts, thereby attaining PLQY values near 100% in some reported systems.^{21–23}

In addition, the organic cations of the 0D OIHMs encapsulate the inorganic clusters to inhibit ion movement and segregation, and enhance stability against external environmental stimuli.²⁴ Given these advantages, emerging 0D OIHMs have demonstrated potential in the production of functional optical devices in various areas. For instance, the majority of Cd²⁺ and Zn²⁺-based halides exhibit blue light emission and typically possess poor quantum luminescence efficiency, whilst Sn²⁺ and Cu⁺-based halides are very prone to oxidation, resulting in stringent preparation and storage requirements.^{25–28} In contrast, In³⁺-based OIHMs are cost-effective, exhibit diverse photoluminescence properties, and demonstrate high luminescence efficiency, making them highly suitable for optical applications such as white LEDs and sensors. Chen *et al.* synthesized the α and β -polymorphs of (DFPD)₂CsInCl₆ using a method that incorporates mixed organic–inorganic cations, achieving PLQYs of 100% and 94% for the [InCl₆]^{3−} octahedral units. Furthermore, both materials demonstrated exceptional thermal stability and uniform colour performance during high-temperature cycling (30–130 °C) and prolonged operation.²⁹ Lei *et al.* synthesized three 0D indium-based halides with near-unity PLQYs.³⁰ As down-conversion phosphors in white LEDs, they generated a soft white light with a CRI above

^aSchool of Physical Science and Technology, State Key Laboratory of Featured Metal Materials and Life-cycle Safety for Composite Structures, Guangxi Key Laboratory of Processing for Non-ferrous Metals and Featured Materials, Guangxi University, Nanning 530004, China

^bResearch Institute of Optoelectronic Functional Materials, School of Chemistry, Chemical Engineering and Materials, Jining University, Qufu, Shandong, 273155, P. R. China

90. Importantly, owing to their disparate solubility in various organic solvents, homogeneous thin films and structured micrometre-scale arrays may be fabricated utilizing solution-based techniques such as spin-coating or spray-coating.

Nevertheless, under intense optical stimulation, 0D indium halides remain susceptible to thermal quenching and increased exciton–phonon interactions, resulting in non-radiative losses that convert photon energy into heat and diminish luminescence efficiency.^{31–34} Maintaining high PLQYs in devices through ecologically friendly production processes remains an unresolved challenge. To address this challenge, numerous strategies are currently under investigation, including the optimisation of crystal structures, the introduction of surface passivation agents, and the development of new synthesis procedures.^{35–40}

In this research, three 0D In^{3+} -based OIHMs were created by carefully adjusting the size and polarity of organic cations using simple solvothermal reactions. Thereafter, the crystalline structures and optical characteristics of these materials were meticulously examined using X-ray diffraction (XRD) and time-resolved photoluminescence (TRPL) spectroscopy, among other methods. The assessments demonstrated the critical role of interactions at the organic–inorganic interface in stabilizing STEs and augmenting emission bandwidths. To evaluate practical applications, the optical performance of these materials was examined in many organic solvents, meticulously analysing luminescence efficiency and longevity over time. These comprehensive studies elucidate the mechanistic principles of interface engineering in enhancing the emission characteristics of 0D indium halides and establish a solid

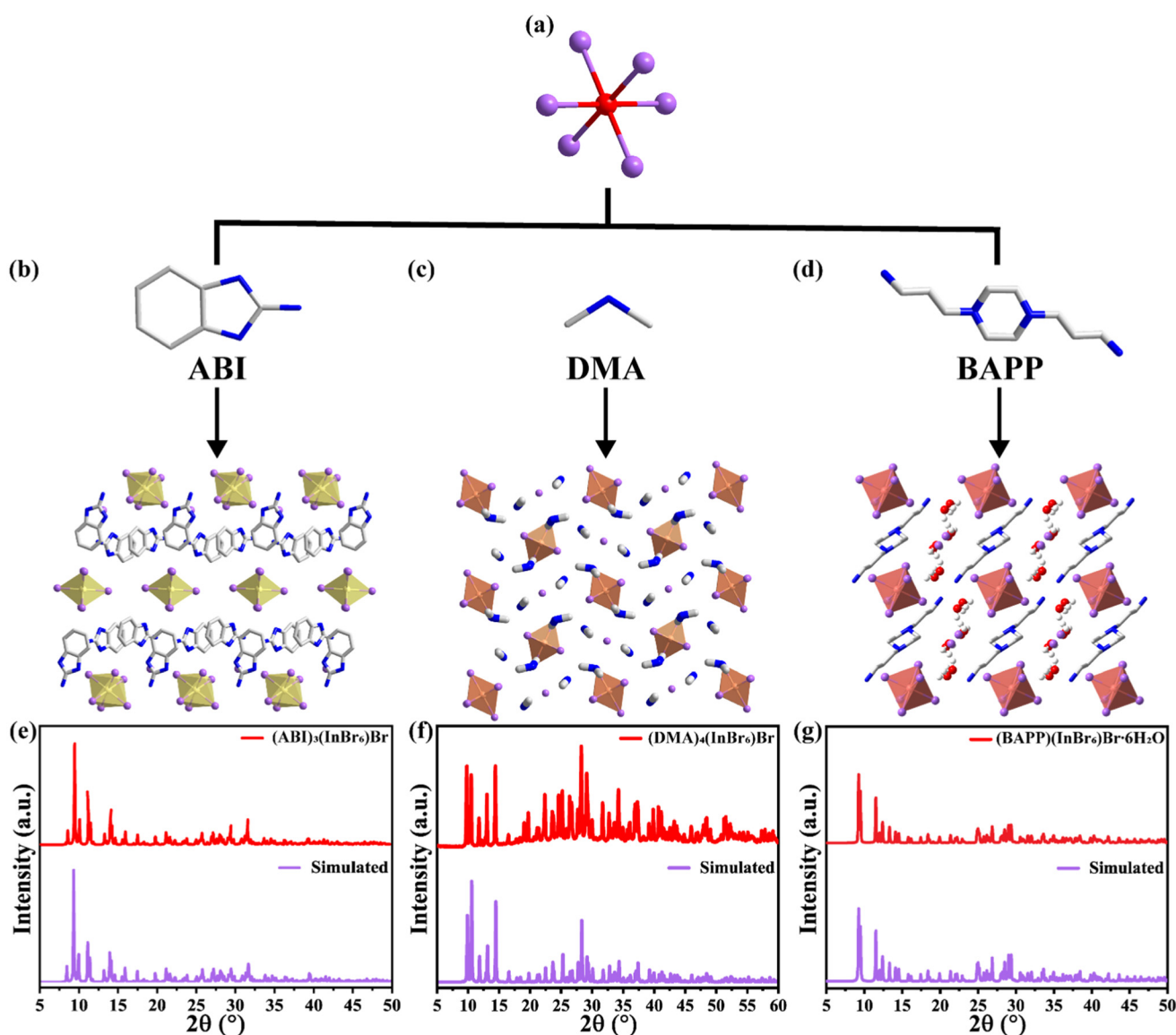


Fig. 1 Crystal structures of three 0D In -based halides: (a) the structure of $[\text{InBr}_6]^{3-}$ octahedra; (b–d) organic cations and packing structures of halides 1–3 (hydrogen atoms are omitted for clarity); (e–g) simulated and experimental PXRD patterns of the three halides.

theoretical and experimental foundation for the advancement of next-generation solid-state lighting materials that provide superior colour rendering and stability.

2. Results and discussion

Single crystals of halides 1–3 were synthesized *via* a solvothermal reaction using the corresponding organic amines, In (AC)₃, and HBr in various solvents. Under the structural-directing influence of different organic cations, each halide adopts a distinct building unit and packing motif. Single-crystal X-ray diffraction (SCXRD) analysis indicated that halide 1 crystallizes in a triclinic crystal system with space group (*P* $\bar{1}$) (Table S1). A central In³⁺ ion is surrounded by six Br[−], creating

a highly symmetrical [InBr₆]^{3−} octahedron with In–Br bond lengths ranging from 2.63(13) to 2.69(11) Å (Table S2), while the Br–In–Br bond angle is about 90° (Fig. S1a). [ABI]⁺ cations arrange in columns along the *b*-axis, encapsulating and stabilizing the isolated [InBr₆]^{3−} units. The presence of π – π stacking interactions between antiparallel-aligned organic cations contributes to enhanced crystal rigidity in the structure (Fig. 1b and Fig. S2).^{41–46} The halides 2 and 3 crystallize in an orthorhombic (*P*₂₁₂₁₂) system and a triclinic (*P* $\bar{1}$) system, respectively, with both structures containing similar octahedral units (Fig. 1a and Tables S1). Free Br[−] ions and water molecules distort the octahedral [InBr₆]^{3−} units in halides 2 and 3, with In–Br bond lengths ranging from 2.65(8)–2.69(6) Å (halide 2) to 2.65(4)–2.69(5) Å (halide 3) (Fig. S1b–S1c, Fig. 1c and d and Tables S3 and S4). These alternating octahedral units assemble

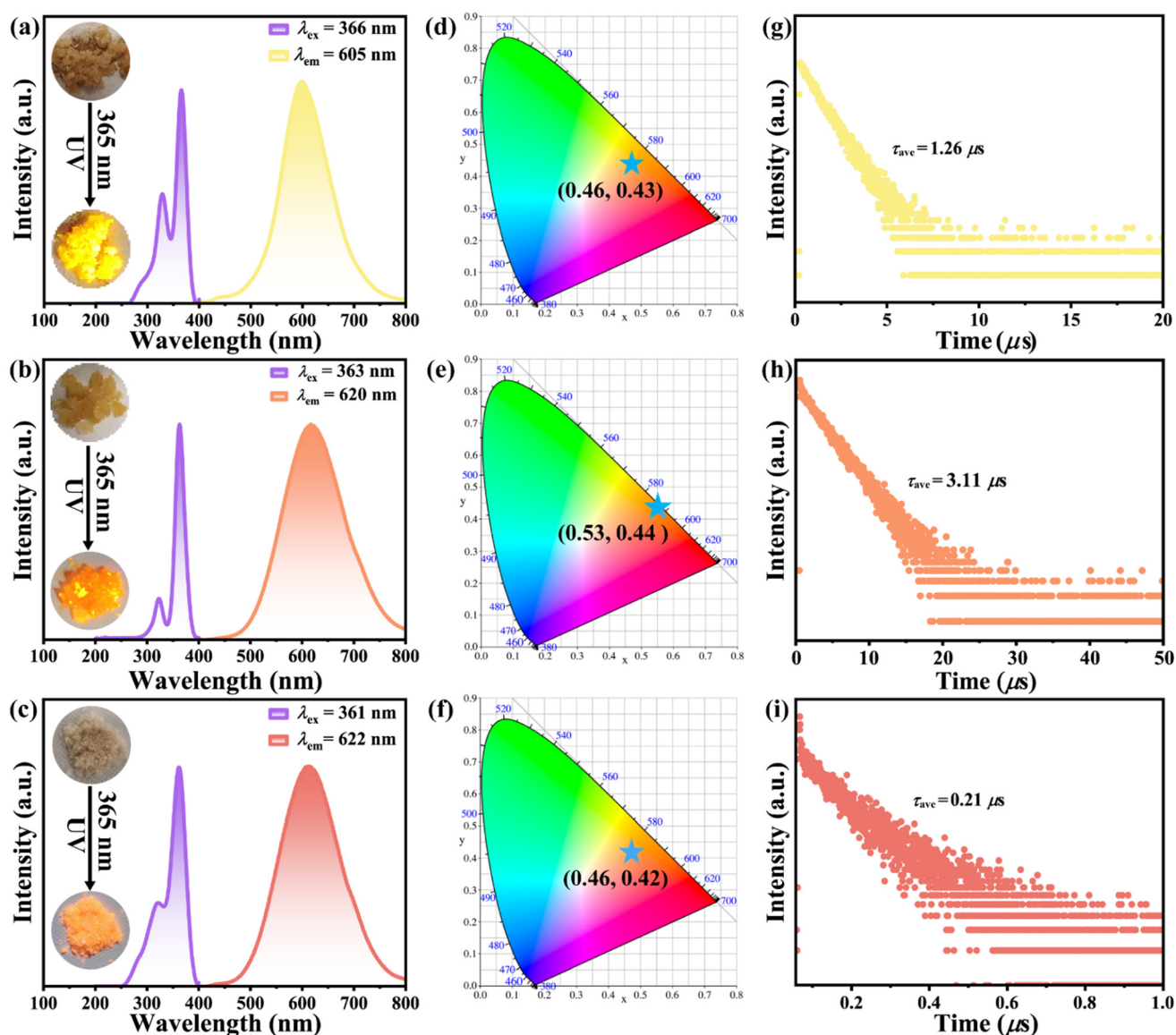


Fig. 2 The PL characterization of halides 1–3: (a–c) PL excitation and emission spectra (inset: photo images of halides under daylight and 365 nm UV light); (d–f) CIE coordinates; (g–i) PL decay curves at room temperature.

into layered sheets, interspersed with organic cations, free Br^- ions, or water molecules, resulting in a hybrid architecture that exhibits long-range ordered 0D characteristics. As illustrated in Fig. 1e–g, the powder X-ray diffraction (PXRD) patterns for the synthesized samples are in perfect agreement with the simulated data derived from single-crystal structures, suggesting the feasibility of the solvothermal reaction method for the synthesis of single crystals of halides 1–3 with high purity.

Subsequently, the optical characteristics of halides 1–3 were investigated. Upon excitation with 365 nm UV light, these crystals exhibited bright yellow to orange light emission. Both the PL excitation and UV–Vis absorption spectra revealed a sharp main peak at 360 nm and a weaker peak at 330 nm. Meanwhile, the wide scattering bands observed beyond 350 nm are linked to interband transitions involving In^{3+} ions (Fig. 2a–c and Fig. S3). When excited at 365 nm, halide 1 emits light at 605 nm, exhibiting a full width at half maxima (FWHM) of 150 nm and a Stokes shift of 239 nm (Fig. 2a). The halides 2 and 3 exhibit emission peaks at 620 nm and 622 nm under the maximum excitation wavelength, respectively (Fig. 2b and c). Notably, while the PL emission intensity varies with excitation wavelength, the emission spectral profiles remain nearly identical in shape and peak position across different monitoring excitation wavelengths (Fig. S4–S6). This consistency suggests that the observed luminescence arises from a single radiation pathway rather than aggregated or

defect-related emission centres. The 3D excitation–emission PL contour map was also constructed, clearly identifying the single emission centre of $[\text{InBr}_6]^{3-}$ (Fig. S7). The Commission Internationale de l'Éclairage (CIE) chromaticity coordinates of these three halides derived from the PL emission spectra are (0.46, 0.43), (0.53, 0.44) and (0.46, 0.42) and fall within the yellow to orange emission areas (Fig. 2d–f). As shown in Fig. S8, halide 1 exhibits a PLQY of 60.80%, which is higher than that of halides 2 (57.74%) and 3 (12.8%). This difference is likely due to the reduced nonradiative transitions caused by the stronger ligand rigidity in halide 1. To elucidate the primary mechanism of emission, PL decay curves for halides 1–3 were recorded under ambient temperature conditions (Fig. 2g–i). The average lifetimes of the materials are 1.26, 3.11, and 0.21 μs , as determined by double-exponential fitting models, aligning with previously reported values for other 0D indium halides linked to the radiative relaxation of STEs.

To further understand the photoluminescence mechanism of these materials, PL emission spectra dependent on temperature were recorded for halide 1 from 80 K to 400 K. As illustrated in Fig. 3a, no peak splitting is detected as the temperature increased, suggesting a single-emission mechanism. It is observed that PL intensities decreased consistently with increasing temperature, which is a feature connected to the lowering of thermally triggered nonradiative recombination due to decreasing lattice vibrations. The activation energy (E_a) is determined by analysing the Arrhenius formula of the inte-

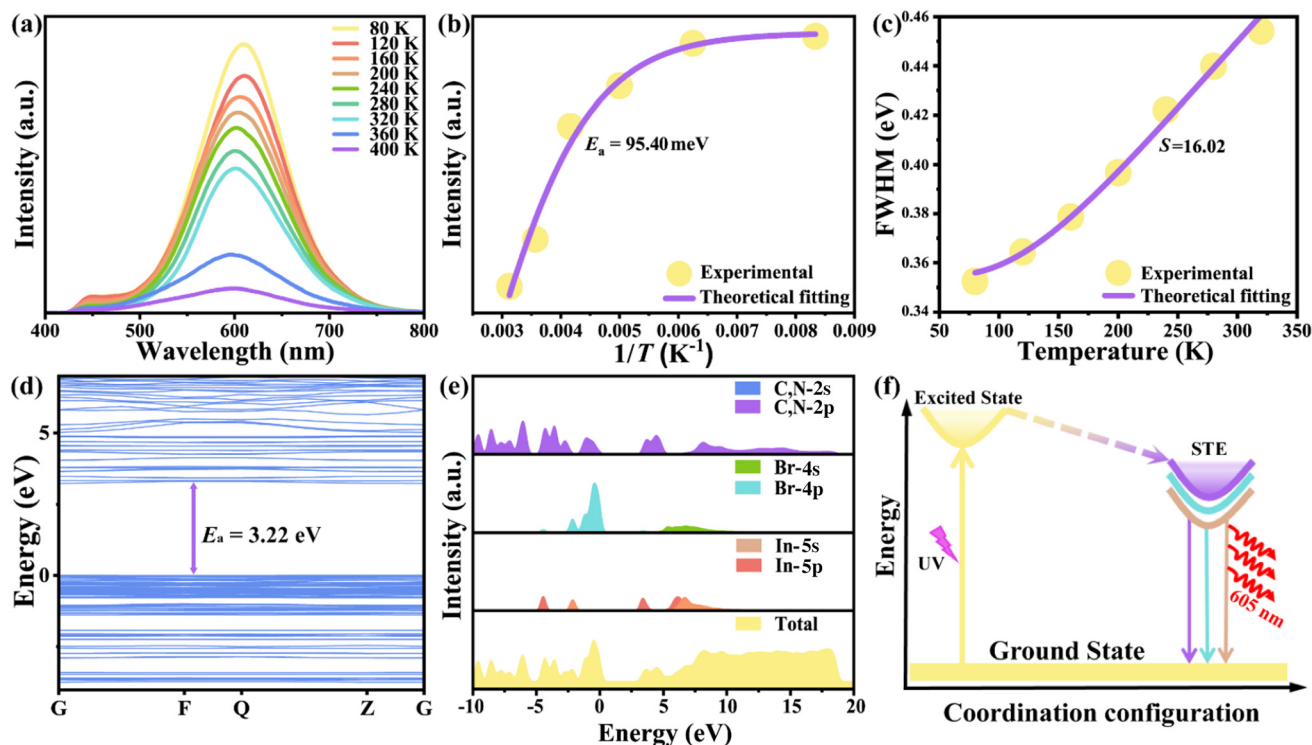


Fig. 3 (a) Temperature-dependent PL emission spectra; (b) integrated PL intensity as a function of reciprocal temperature; (c) fitted plot of PL FWHM versus the temperature of halide 1; (d) calculated band structure and (e) DOS of halide 1; (f) configuration diagram of the emission process of halide 1.

grated photoluminescence intensity against the reciprocal of the temperature, thereby quantifying the thermal quenching effect:

$$I(T) = \frac{I(0 \text{ K})}{1 + A \exp\left(\frac{E_a}{k_B T}\right)}$$

where $I(T)$ and $I(0 \text{ K})$ denote the integrated photoluminescence intensities at $T \text{ K}$ and 0 K , respectively. The obtained E_a value of 95.40 meV for halide **1** surpasses the thermal dissociation energy ($\sim 26 \text{ meV}$) of bound excitons at 300 K , thereby affirming the ease of STE formation and effective radiative recombination upon photoexcitation (Fig. 3b). Simultaneously, it was noted that as the temperature increased from 80 K to 300 K , the FWHM of the emission bands became wider, indicating stronger electron–phonon coupling resulting from increased lattice vibrations. The intensity of electron–phonon interactions can be assessed with the Huang–Rhys factor (S) as follows:

$$\text{FWHM}(T) = 2.36\sqrt{S} \times E_{\text{ph}} \left[\coth\left(\frac{E_{\text{ph}}}{2k_B T}\right) \right]^{1/2}$$

where E_{ph} represents the mean phonon energy, T denotes the temperature measured in Kelvin (K), and k_B refers to the

Boltzmann constant. The substantial S value of 16.02 suggests a significant electron–phonon interaction within a soft crystal lattice, which corresponds to a wide FWHM exceeding 150 nm and a Stokes shift of 239 nm (Fig. 3c). Subsequently, calculations utilizing density functional theory (DFT) were conducted on halide **1** to achieve a deeper comprehension of its electronic configuration. As illustrated in Fig. 3d and Fig. S9, a direct bandgap measuring 3.22 eV is determined, which is marginally lower than that suggested by UV–Vis absorption due to the underestimated bandgap. Notably, very flat bands close to the Fermi level are identified, indicating the presence of strongly localized states and significant quantum confinement that facilitates exciton trapping. Analysis of both the total and partial density of states (Fig. 3e) indicates that the maxima of the valence band are primarily influenced by Br $4p$ orbitals, while the minima of the conduction band are predominantly derived from $\text{In}^{3+} 5s$ states, with minimal involvement from the organic cations. Together, the findings from experiments and theoretical modelling suggest an emission mechanism wherein high-energy UV excitation creates localized triple-state free excitons, which are then swiftly trapped by a flexible, deformable lattice through strong electron–phonon coupling. This process leads to intersystem crossing, resulting in the formation of lower-energy STEs. The subsequent radiative relaxation of these STEs back to the ground

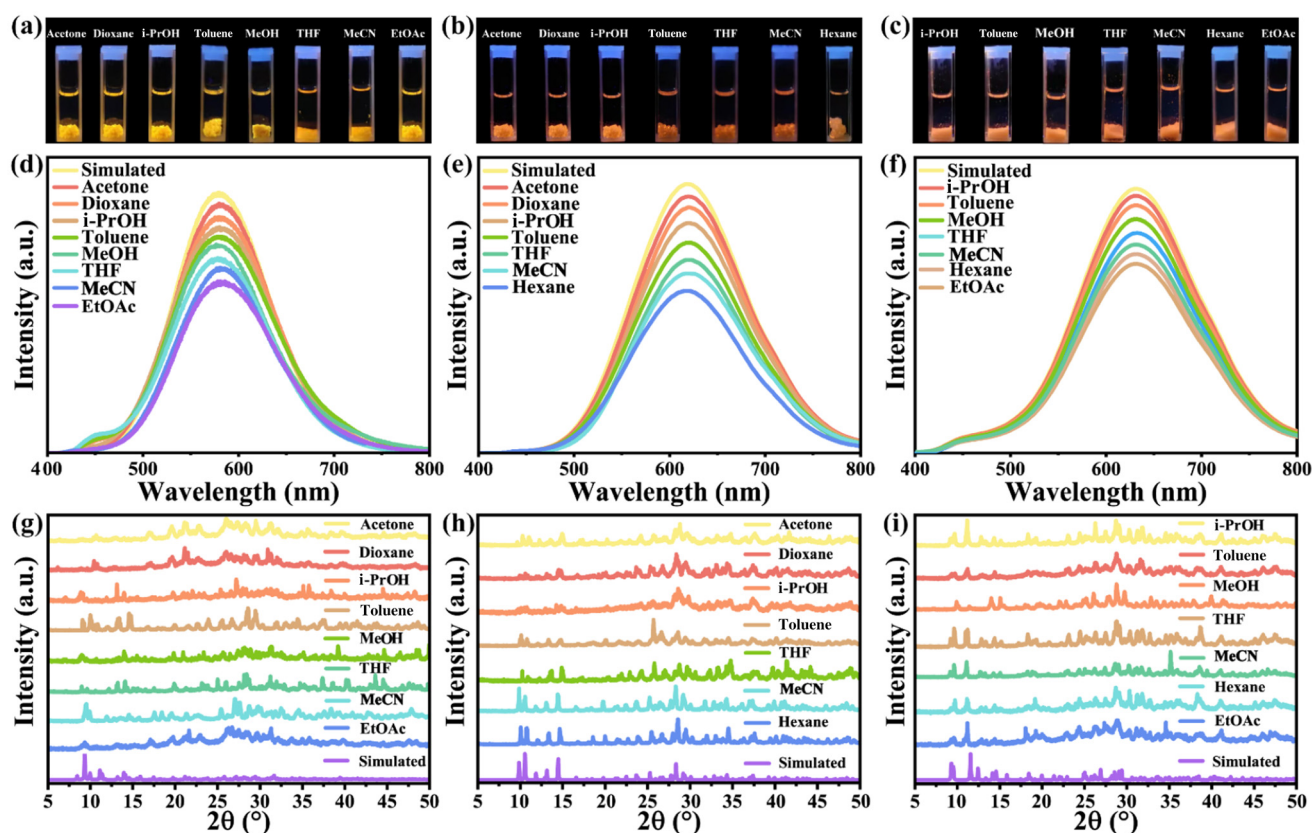


Fig. 4 Stabilities of the halide crystals after soaking in polar solvents for 7 days. (a–c) Photographs taken under 365 nm UV light of halides 1–3. (d–f) PL spectra of halides 1–3. (g–i) XRD patterns of halides 1–3.

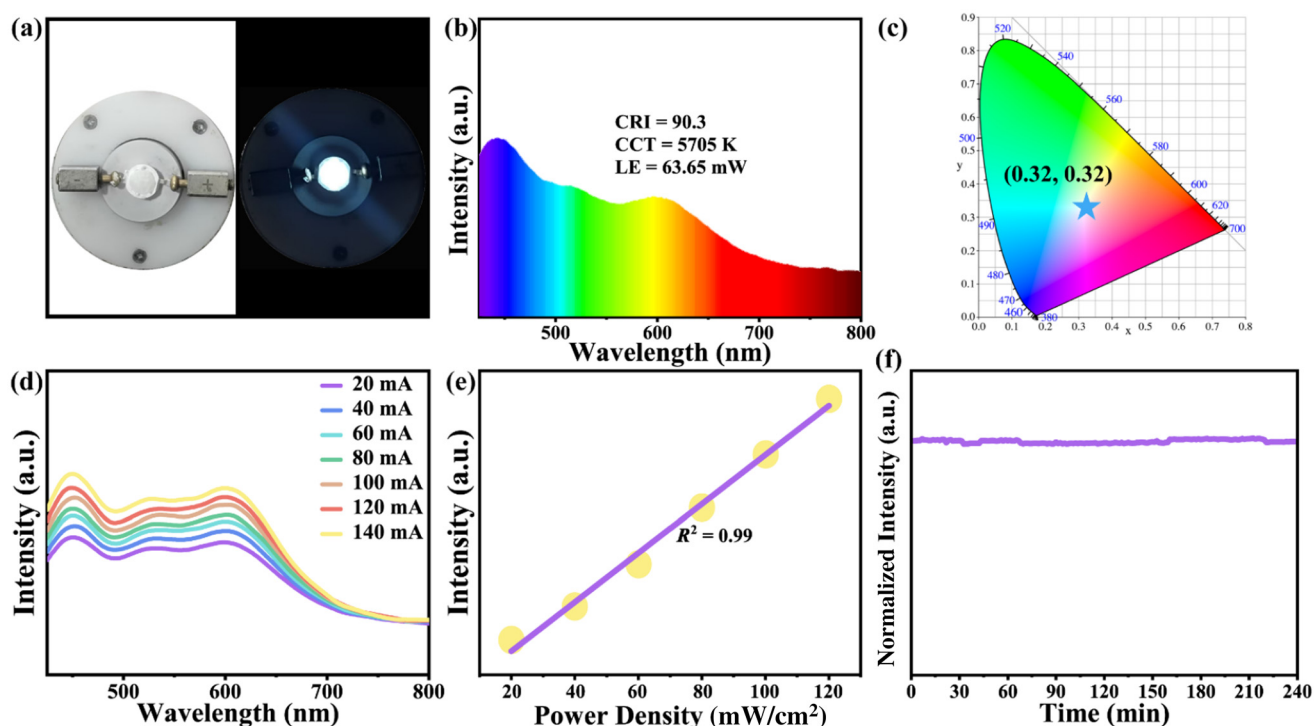


Fig. 5 (a) Photographs of the WLED. (b) PL spectrum of the WLED. (c) CIE coordinates of the WLED. (d) PL spectra of the WLED under various currents. (e) Intensity and (f) efficiency profiles of the WLED.

state is responsible for the observed broad-spectrum visible emission, as depicted in the configuration coordinate diagram (Fig. 3f).

The stability of powders of halides 1–3 is assessed by immersing them in various polar and nonpolar solvents, such as acetone, dioxane, *i*-PrOH, toluene, MeOH, THF, MeCN, and EtOAc. After 7 days, these materials maintained sedimentation without any significant suspension of material or phase separation (Fig. 4a–c), and no colour change was detected on the surface of the powders, demonstrating solvent-resistant stability. The PL spectra illustrated in Fig. 4d–f reveal uniform emission at identical wavelengths, with very minor variations in the emission peaks and their intensities. The PXRD patterns depicted in Fig. 4g–i closely correspond to the simulated profiles from single-crystal diffraction, exhibiting no shifts or diminutions in the principal peaks. This finding suggests that the crystal phases were preserved across all chemical environments.

The stability characteristics of the materials prompted us to explore their applications in optoelectronic materials such as solid-state white LEDs. The yellow-emission halide **1** is mixed with the commercial green phosphor (Ba,Sr)SiO₄:Eu²⁺ and blue phosphor (Sr,Ca)₂SiO₄:Eu²⁺ in appropriate proportions and deposited onto a 365 nm UV chip (Fig. 5a). As illustrated in Fig. 5b and 5c, the optical device emitted a soft white light with a CRI of 90.3, a CCT of 5705 K, and CIE coordinates of (0.32, 0.32) at a current of 20 mA, demonstrating minimal colour bias and outstanding visual quality (Fig. 5b and c). To

evaluate the stability of the LED, the emission intensity was first tested under different currents. As the driving current was increased from 20 to 140 mA, the intensities of both PL peaks were elevated proportionally, with no evidence of energy transfer or self-absorption occurring between the three phosphors, thus showcasing stable performance during high-power operation (Fig. 5d and e). Significantly, following numerous hours of uninterrupted operation, the luminous efficacy and colour attributes of the LED remained virtually consistent, further affirming its remarkable long-term stability (Fig. 5f). These 0D hybrid indium halides have the potential to be utilized as highly effective down-conversion yellow phosphors in white LEDs, providing outstanding luminescence performance, and superior colour quality and durability, thereby presenting a solution for the progression of next-generation solid-state lighting technologies.

3. Conclusions

In conclusion, three novel 0D hybrid indium bromides were synthesized, exhibiting persistent emission across yellow ($\lambda = 605$ nm) to orange ($\lambda = 622$ nm) wavelengths with remarkable PLQY of up to 60.8%. Theoretical studies indicate a direct bandgap of around 3.22 eV and the existence of localized electronic states, suggesting that the extensive emission results from the radiative relaxation of self-trapped excitons. The remarkable stability of these materials, demonstrated by

various solvent immersion tests, underscores their suitability for optoelectronic applications. When employed as down-conversion phosphors in white LEDs, they provide soft white light with excellent colour rendering (CRI > 90) and exhibit stable performance over variable currents and extended operation times. These findings conclusively identify 0D indium halides as viable options for dependable and efficient emitters in advanced solid-state lighting technologies.

4. Experimental

Materials

All materials used in the experiments were sourced directly from commercial suppliers and did not undergo further purification. The chemicals utilized include In(AC)₃ (99%, Meryer), HBr (40%, Macklin), 2-aminobenzimidazole (97%, Macklin), dimethylamine (97%, Macklin), 1,4-bis(3-aminopropyl)piperazine (99%, Aladdin), ethyl alcohol (99%, Macklin), and propan-2-ol (99%, Macklin).

Synthesis of (ABI)₃(InBr₆)Br (halide 1)

A mixture of 2-aminobenzimidazole (2 mmol, 0.4 g), In(AC)₃ (1 mmol, 0.291 g), HBr (2 mL), and propan-2-ol (2 mL) was prepared and transferred into a 25 mL glass vial. The solution was subjected to sonication under ambient temperature conditions for 10 minutes and subsequently heated at 80 °C for a duration of five days. Analysis using SCXRD indicated that the halide structure corresponds to (ABI)₃(InBr₆)Br.

Synthesis of (DMA)₄(InBr₆)Br (halide 2)

A combination of DMF (2 mL), In(AC)₃ (1 mmol, 0.291 g), dimethylamine (1 mmol, 0.101 g) and HBr (2 mL) was created and moved into a 25 mL glass vial. The solution was subjected to sonication under ambient temperature conditions for 10 minutes and subsequently heated at 80 °C for a duration of five days. Analysis using SCXRD indicated that the halide structure corresponds to (DMA)₄(InBr₆)Br.

Synthesis of (BAPP)(InBr₆)Br·6H₂O (halide 3)

1,4-Bis(3-aminopropyl)piperazine (1 mmol, 0.2 g), In(AC)₃ (1 mmol, 0.291 g), HBr (2 mL), and ethyl alcohol (2 mL) were added into a 25 mL glass vial. The mixture was subjected to sonication under ambient temperature conditions for 10 minutes and subsequently heated at 80 °C for a duration of five days. Analysis using SCXRD indicated that the halide structure corresponds to (BAPP)(InBr₆)Br·6H₂O.

Single-crystal X-ray diffraction

A Bruker D8 Quest diffractometer, using Mo K α radiation (λ = 0.71073 Å), was utilized to gather SCXRD data for halides 1–3 at temperatures of 273 K, 273 K, and 293 K, respectively. The determination and refinement of the crystal structures were performed with the SHELXL program within the OLEX2 software framework. The crystal data, bond angles, and bond lengths for halides 1–3 are detailed in Tables S1–S4. Reference

numbers from the Cambridge Crystallographic Data Centre (CCDC) include 2445848 for (C₈H₃₂N₄InBr₇), 2445847 for (C₂₁H₂₄N₉InBr₇), and 2445846 for (C₁₀H₄₀N₄O₆InBr₇).

PL property characterization studies

An FLS980 fluorescence spectrometer was used to capture photoluminescence excitation (PLE) and emission (PL) spectra, featuring an integrated sphere to evaluate the PLQY. The calculation of PLQY followed the equation $\eta_{\text{QE}} = I_{\text{s}}/(E_{\text{R}} - E_{\text{s}})$, where I_{s} refers to the emission spectrum from a single sample, E_{s} indicates the excitation spectrum of that individual sample, and E_{R} represents the excitation spectrum obtained from an empty integrating sphere without a sample. Additionally, the Edinburgh FLS980 fluorescence spectrometer, which includes a picosecond-pulsed diode laser, facilitated the acquisition of time-resolved decay data. These data were analysed with a monoexponential function to ascertain the fluorescence lifetime. The chromaticity coordinates, as defined by the Commission Internationale de l'Éclairage (CIE), were derived from the PL emission spectrum.

Structure–property characterization studies

A Bruker D8 ADVANCE powder X-ray diffractometer was utilized to conduct powder X-ray diffraction (PXRD). Diffraction patterns for the compounds were recorded by sweeping the sample through an angular range of 5–60° (2 θ) at room temperature, operating at 40 kV and 40 mA, with a scanning speed of 10° per minute.

Theoretical calculations

Based on density functional theory, the theoretical calculations for the title compounds were performed using the total energy code of the Cambridge Sequential Total Energy Package (CASTEP) software. Norm-conserving pseudopotentials could be used for describing the relationship between ionic cores and electrons. Hence, valence electrons adopt C 2s²2p², N 2s²2p³, In 5s²5p¹, and Br 4s²4p⁵ configurations. Finally, the CASTEP code provides default values of essential convergence criteria and calculation parameters.

Fabrication of the WLED

The red (ABI)₃(InBr₆)Br phosphor, commercial green phosphor of (Ba,Sr)SiO₄:Eu²⁺, and commercial blue phosphor of (Sr,Ca)₂SiO₄:Eu²⁺ were thoroughly mixed using an epoxy resin. The LED chip was subsequently coated with the resulting mixture. Using an integrating sphere spectroradiometer system (EVERFINE HAAS-2000), measurements were taken for the electrical and photoelectric characteristics, including the emission spectrum, colour temperature (CCT), CRI (R_{a}), and CIE colour coordinates of the LED. The white LED was tested at 3 V with a range of drive currents varying from 20 to 120 mA.

Conflicts of interest

The authors declare no conflict of interest.

Data availability

The data that support the findings of this study are available in the SI of this article.

Additional characterizations of three compounds, including UV-vis absorption spectra, PLQY, PL spectroscopy data, and $\pi\cdots\pi$ stacking characterization are provided in the SI. See DOI: <https://doi.org/10.1039/d5dt01382h>.

CCDC 2445846–2445848 contain the supplementary crystallographic data for this paper.^{47a–c}

Acknowledgements

We express thanks for financial support from the National Natural Science Foundation of China (22171105 and 22471096), the Shandong Provincial Natural Science Foundation (ZR2022YQ14, ZR2022QB127, and ZR2022QB221), the Special Foundation of Taishan Scholar Project and Young Innovative Team Project for Colleges and Universities of Shandong Province (2024KJH053).

References

- 1 D. Chen, J. Li, X. Chen, J. Chen and J. Zhong, *ACS Appl. Mater. Interfaces*, 2019, **11**, 10059–10067.
- 2 Y. Liu, Y. Ying, Q. Xie, Z. Gao, X. Shao, M. Zhou, W. Pei, X. Tang and Y. Tu, *Inorg. Chem.*, 2024, **63**, 16167–16176.
- 3 J. Zhang, T. Zhang, Z. Ma, F. Yuan, X. Zhou, H. Wang, Z. Liu, J. Qing, H. Chen, X. Li, S. Su, J. Xie, Z. Shi, L. Hou and C. Shan, *Adv. Mater.*, 2023, **35**, 2209002.
- 4 Y.-Y. Guo and P. Lightfoot, *Dalton Trans.*, 2020, **49**, 12767–12775.
- 5 S. Seth, T. Ahmed, A. De and A. Samanta, *ACS Energy Lett.*, 2019, **4**, 1610–1618.
- 6 A. Pan, M. Jurow, Y. Zhao, F. Qiu, Y. Liu, J. Yang, J. J. Urban, L. He and Y. Liu, *Nanoscale*, 2017, **9**, 17688–17693.
- 7 X. Song, S. Wang, Y. Yang, Y. Zhou, X. Huang, B. Tang and H. Liu, *Chem. Mater.*, 2024, **36**, 7744–7753.
- 8 Y. Tong, X. Bi, S. Xu, H. Min, L. Cheng, Z. Kuang, L. Yuan, F. Zhou, Y. Chu, L. Xu, L. Zhu, N. Zhao, N. Wang, W. Huang and J. Wang, *Adv. Mater.*, 2023, **35**, 2207111.
- 9 Q. Zhang, D. Zhang, B. Cao, S. Poddar, X. Mo and Z. Fan, *ACS Nano*, 2024, **18**, 8557–8570.
- 10 L. Xie, Z. Liu, H. Yang, K. Chen, N. Lv, H. Pi, X. Chen, X. Li, Z. Liu, S. Li, Z. Wang, Y. Wang and B. Chen, *Adv. Opt. Mater.*, 2024, **12**, 2401050.
- 11 S. Wang, X. Sun, J. Shi, R. Zhao, B. Zhang, S. Lu, P. Li, F. Li, L. Manna, Y. Zhang and Y. Song, *Adv. Mater.*, 2024, **36**, 2413673.
- 12 V. R. F. Schroeder, N. Fratzscher, N. Z. Morales, D. S. Ruehl, F. Hermerschmidt, E. L. Unger and E. J. W. List-Kratochvil, *Mater. Horiz.*, 2024, **11**, 1989–1996.
- 13 J. Ren, H. Liu, X. Zhou, G. Zhang, G. Yan, F. Liu, L. Chen and Y. Wang, *Chem. Eng. J.*, 2024, **488**, 150977.
- 14 D. A. Popy, Y. Singh, Y. Tratsiak, A. M. Cardoza, J. M. Lane, L. Stand, M. Zhuravleva, N. Rai and B. Saparov, *Aggregate*, 2024, **5**, e602.
- 15 J. a. Lai, C. Li, Z. Wang, L. Guo, Y. Wang, K. An, S. Cao, D. Wu, Z. Liu, Z. Hu, Y. Leng, J. Du, P. He and X. Tang, *Chem. Eng. J.*, 2024, **494**, 153077.
- 16 D. Ju, M. Zhou, Z. Liu, P. Ran, Z. Dong, S. Hou, H. Li, W. Xiao, X. Xu, H. Li, Y. Yang and T. Jiang, *Small*, 2024, **20**, 2305083.
- 17 Y. Xing, H. He, Z. Cui, Z. Fu, S. Qin, W. Zhang, S. Mei and R. Guo, *Adv. Opt. Mater.*, 2024, **12**, 2302679.
- 18 X. Meng, J. Jiang, X. Yang, H. Zhao, Q. Meng, Y. Bai, Q. Wang, J. Song, C. Katan, J. Even, W. W. Yu and F. Liu, *Angew. Chem., Int. Ed.*, 2024, **63**, e202411047.
- 19 Y. Wu, X.-M. Zhen and B. Zhang, *Inorg. Chem.*, 2023, **62**, 19573–19581.
- 20 X. Cheng, Y. Han, T. Cheng, Y. Xie, X. Chang, Y. Lin, L. Lv, J. Li, J. Yin and B.-B. Cui, *ACS Appl. Mater. Interfaces*, 2023, **15**, 32506–32514.
- 21 G. Zhang, P. Dang, H. Lian, K. Li, L. Tian, W. Yang, Z. Cheng and J. Lin, *Laser Photonics Rev.*, 2024, **18**, 2300599.
- 22 X. Wang, T. Bai, J. Sun, J. Liu, Y. Su and J. Chen, *Chem. Eng. J.*, 2024, **486**, 150257.
- 23 Y. Bai, S. Zhang, N. Luo, B. Zou and R. Zeng, *Nano Res.*, 2024, **17**, 7768–7775.
- 24 F. Zhao, J. Bae, X. Zhou, Y. Guo and G. Yu, *Adv. Mater.*, 2018, **30**, 1801796.
- 25 H. Liu, T. B. Shonde, F. Gonzalez, O. J. Olasupo, S. Lee, D. Luong, X. Lin, J. S. R. v. Winfred, E. Lochner, I. Fatima, K. Hanson and B. Ma, *Adv. Mater.*, 2023, **35**, 2209417.
- 26 N. Lin, R. C. Wang, S. Y. Zhang, Z. H. Lin, X. Y. Chen, Z. N. Li, X. W. Lei, Y. Y. Wang and C. Y. Yue, *Laser Photonics Rev.*, 2023, **17**, 7768–7775.
- 27 B. Su, J. Jin, K. Han and Z. Xia, *Adv. Funct. Mater.*, 2022, **33**, 2210735.
- 28 X. Meng, S. Ji, Q. Wang, X. Wang, T. Bai, R. Zhang, B. Yang, Y. Li, Z. Shao, J. Jiang, K. I. Han and F. Liu, *Adv. Sci.*, 2022, **9**, 2203596.
- 29 Z. Tang, X. Wang, T. Bai, S. Liu, S. Wang, Q. Wei, B. Fan and J. Chen, *Adv. Opt. Mater.*, 2024, **13**, 2402409.
- 30 Q. Wang, W. Jiang, T.-C. Liu, H.-R. Liu, R.-R. Hu, W.-X. Sun, F.-T. Guo, B. Hu and X.-W. Lei, *ACS Appl. Mater. Interfaces*, 2025, **17**, 24048–24057.
- 31 P. Yang, C. Yang, Z. Wu and Z. Tang, *Matter*, 2025, **8**, 102046.
- 32 B. Lyu, H. Lin, D. Li, A. Sergeev, Q. Wang, Z. Jiang, L. Huo, H. Su, K. S. Wong, Y. Wang and W. C. H. Choy, *ACS Energy Lett.*, 2024, **9**, 2118–2127.
- 33 W. H. Jeong, S. Lee, H. Song, X. Shen, H. Choi, Y. Choi, J. Yang, J. W. Yoon, Z. Yu, J. Kim, G. E. Seok, J. Lee, H. Y. Kim, H. J. Snaith, H. Choi, S. H. Park and B. R. Lee, *Adv. Sci.*, 2024, **11**, 2305383.
- 34 Y. Gao, Q. Cai, Y. He, D. Zhang, Q. Cao, M. Zhu, Z. Ma, B. Zhao, H. He, D. Di, Z. Ye and X. Dai, *Sci. Adv.*, 2024, **10**, 5645.

- 35 S.-Q. Sun, Q. Sun, Y.-J. Ji, Y.-L. Xu, W. He, M. Zhu, J.-G. Zhou, Y.-J. Yu, D.-D. Feng, Y.-M. Xie, Y.-Y. Li and M.-K. Fung, *Small*, 2023, **19**, 2400421.
- 36 A. Ray, L. De Trizio, J. Zito, I. Infante, L. Manna and A. L. L. Abdelhady, *Adv. Opt. Mater.*, 2023, **11**, 2202005.
- 37 Y. Jiang, K. Wei, C. Sun, Y. Feng, L. Zhang, M. Cui, S. Li, W.-D. Li, J. T. Kim, C. Qin and M. Yuan, *Adv. Mater.*, 2023, **35**, 2304094.
- 38 W. Huang, X. Wu, B. Ahmed, Y. Li, Y. Zhou, H. Wang, Y. Song, X. Kuang, J. Luo and S. Zhao, *Inorg. Chem. Front.*, 2023, **10**, 2039–2044.
- 39 Z. Chen, X.-K. Liu, H. Wang, X. Liu, L. Hou and F. Gao, *Adv. Opt. Mater.*, 2023, **11**, 2202528.
- 40 S.-D. Baek, C. Wang, D.-Y. Khang and J.-M. Myoung, *Chem. Eng. J.*, 2023, **455**, 140594.
- 41 Y. Ye, L. Yao and G. Liu, *Chin. J. Struct. Chem.*, 2025, **44**, 100460.
- 42 H. Qiu, S. Yang, M. Li, H. Chen, Y. Zhang, X. Chen and Y. Zheng, *Inorg. Chem. Front.*, 2025, **12**, 637–646.
- 43 K. Kim, Y. Li and K. M. Ok, *J. Am. Chem. Soc.*, 2025, **147**, 2880–2888.
- 44 J. Q. Zhao, D. Y. Wang, T. Y. Yan, Y. F. Wu, Z. L. Gong, Z. W. Chen, C. Y. Yue, D. Yan and X. W. Lei, *Angew. Chem., Int. Ed.*, 2024, **63**, e202412350.
- 45 K. Zhang, S. Chen, X. Zhang, B. Wang and X. Li, *Chem. Eng. J.*, 2024, **489**, 151317.
- 46 W. Yang, P. Dang, G. Zhang, D. Liu, Y. Wang, Y. Wei, H. Lian, G. Li and J. Lin, *Angew. Chem., Int. Ed.*, 2024, **63**, e202411136.
- 47 (a) H. Z. Zan, X. Z. Wang, H. X. Zhao, S. W. Wang, L. Chen, H. Y. Wang, L. Z. Zhao, X. D. Zhang and X. W. Kong, CCDC 2445846: Experimental Crystal Structure Determination, 2025, DOI: [10.5517/ccdc.csd.cc2n3385](https://doi.org/10.5517/ccdc.csd.cc2n3385); (b) H. Z. Zan, X. Z. Wang, H. X. Zhao, S. W. Wang, L. Chen, H. Y. Wang, L. Z. Zhao, X. D. Zhang and X. W. Kong, CCDC 2445847: Experimental Crystal Structure Determination, 2025, DOI: [10.5517/ccdc.csd.cc2n3396](https://doi.org/10.5517/ccdc.csd.cc2n3396); (c) H. Z. Zan, X. Z. Wang, H. X. Zhao, S. W. Wang, L. Chen, H. Y. Wang, L. Z. Zhao, X. D. Zhang and X. W. Kong, CCDC 2445848: Experimental Crystal Structure Determination, 2025, DOI: [10.5517/ccdc.csd.cc2n33b7](https://doi.org/10.5517/ccdc.csd.cc2n33b7).